


ARTICLE

<https://doi.org/10.1038/s42005-019-0213-x>

OPEN

Multipolar terahertz absorption spectroscopy ignited by graphene plasmons

Alessandro Ciattoni ¹, Claudio Conti^{2,3} & Andrea Marini⁴

Terahertz absorption spectroscopy plays a key role in physical, chemical and biological systems as a powerful tool to identify molecular species through their rotational spectrum fingerprint. Owing to the sub-nanometer scale of molecules, radiation-matter coupling is typically dominated by dipolar interaction. Here we show that multipolar rotational spectroscopy of molecules in proximity of localized graphene structures can be accessed through the extraordinary enhancement of their multipolar transitions provided by terahertz plasmons. In particular, specializing our calculations to homonuclear diatomic molecules, we demonstrate that a micron-sized graphene ring with a nano-hole at the core combines a strong near-field enhancement and an inherently pronounced field localization enabling the enhancement of the dipole-forbidden terahertz absorption cross-section of H_2^+ by 8 orders of magnitude. Our results shed light on the strong potential offered by nano-structured graphene as a robust and electrically tunable platform for multipolar terahertz absorption spectroscopy at the nanoscale.

¹CNR-SPIN, c/o Dip.to di Scienze Fisiche e Chimiche - Via Vetoio, 67010 Coppito (AQ), Italy. ²Consiglio Nazionale delle Ricerche, CNR-ISC, Via dei Taurini 19, 00185 Rome, Italy. ³Department of Physics, University Sapienza, Piazzale Aldo Moro 5, 00185 Rome, Italy. ⁴Department of Physical and Chemical Sciences, University of L'Aquila, Via Vetoio, 67100 L'Aquila, Italy. Correspondence and requests for materials should be addressed to A.C. (email: alessandro.ciattoni@aquila.infn.it) or to A.M. (email: andrea.marini@aquila.infn.it)

The terahertz (THz) domain of the electromagnetic radiation spectrum hosts a plethora of complex mechanisms entailing radiation–matter interaction in physical^{1–4}, chemical^{5–9}, and biological^{10–12} systems. THz radiation plays a key role in noninvasive medical diagnostics because of the low photon energy (\simeq meV) that does not lead to ionization, thus not posing at risk living organisms and enabling imaging of the tooth structure, skin cancer, and tumors^{13,14}. Furthermore, structural vibrations and rotations of molecules involve absorption resonances in the THz spectrum playing the role of peculiar barcodes enabling chemical identification of substances in security screening, food, and pharmaceutical inspection. In this respect, THz absorption spectroscopy entails the chemical resolution of dangerous and illicit substances concealed within dry packaging like pure and plastic explosives¹⁵, MDMA (ecstasy)¹⁶, methamphetamine hydrochloride¹⁷, and ephedrine¹⁸.

Generally, because the typical size of molecules is much smaller than the radiation wavelength, their effective interaction with radiation is rather weak and occurs within the so-called dipole approximation, which assumes molecules as point-like scatterers so that the spatial variation of the radiation field can be disregarded within the volume of the molecule itself. In the context of molecular rotational spectroscopy, the dipole-like radiation–molecule interaction implies that molecules should possess a permanent dipole moment and absorption among rotational levels occurs only for well-known selection rules $\Delta J = \pm 1$ and $\Delta M = 0, \pm 1$, where J, M are the norm and azimuthal rotational quantum numbers of the molecule¹⁹. Such selection rules limit the amount of information extractable from molecular absorption spectra. Furthermore, symmetric molecules that do not possess a permanent dipole moment do not absorb, and can not be probed by THz radiation.

Nanophotonics offers a platform to increase radiation–molecule interaction through the tight confinement and large field enhancement produced by plasmons, i.e., the collective excitations of conduction electrons in metals, thus enabling surface-enhanced infrared absorption (SEIRA) and surface-enhanced Raman scattering (SERS)^{20,21}. Both SERS and SEIRA enable chemical resolution with a sensitivity that can reach the single-molecule detection limit^{22–24}, and have been exploited for several applications like pregnancy tests based on metal colloids²⁵ and cancer screening²⁶. The lower photon energy in surface-enhanced THz absorption spectroscopy (SETAS) further enables the noninvasive chemical resolution of polymers and proteins²⁷. Doped graphene offers an appealing alternative to noble metals because it sustains electrically tunable surface plasmons at infrared and THz frequencies^{28–33}, thus enabling label-free SERS and SEIRA^{34–39}.

Here, we explore the potential of localized graphene plasmons for multipolar SETAS of dipole-inactive molecules. In particular, we demonstrate that the strong-field enhancement and the deep-subwavelength features of THz plasmons in a graphene micro-ring with a nano-hole at the core generate sharp peaks at the inner and outer edges such that the multipolar absorption cross-section of nearby molecules increases enormously. Specializing our calculations to the simplest dipole-inactive homonuclear diatomic molecule, i.e., H_2^+ , we observe that its plasmon-enhanced average quadrupolar absorption cross-section increases up to eight orders of magnitude with respect to homogeneous plane-wave excitation. Our calculations based on frequency-domain modeling of graphene plasmons in the random phase approximation (RPA) and Power–Zienau–Woolley radiation–molecule interaction further illustrate the detailed angular momentum exchange between the molecule and the impinging radiation, unveiling that plasmon-enhanced radiation spin–orbit interaction⁴⁰ opens transition channels for all

molecular orientations. Our results constitute a solid theoretical basis to support graphene as an ideal platform for electrically tunable multipolar SETAS at the nanoscale.

Results

Terahertz graphene plasmons. Because multipolar absorption spectroscopy relies on field localization, it is essential to excite dipole-inactive molecules with deep-subwavelength THz fields. Surface plasmons in metal-based⁴¹ and graphene-based⁴² waveguides and localized structures are crucial in this context because they enable strong-field localization well below the wavelength. The appeal of graphene stems from its linear energy dispersion $\mathcal{E} = v_F k_e$ for low-energy electrons with wave vector \mathbf{k}_e , where $v_F \simeq c/300$ is the Fermi velocity and c is the speed of light in vacuum. Thanks to such linear dispersion, electrical doping through an external bias voltage enables a substantial shift of the Fermi energy up to $\simeq 1$ eV⁴³. In turn, while metal-based structures possess fixed resonances lacking post-fabrication tunability, graphene overcomes this limit through electrical gating. Furthermore, graphene plasmons have an effective wavelength λ_{eff} that can reach $\lambda_{\text{eff}} \simeq \lambda/100$ (where λ is the vacuum wavelength) along with reduced absorption and thus are superior to metals in terms of field localization and resonance quality factor^{44–46}. Our theoretical description of the graphene response to Terahertz waves is based on the local random phase approximation (RPA) (see Supplementary Note 1), with an experimentally realistic electron mobility set to $\mu = 1 \text{ m}^2 \text{ V}^{-1} \text{ s}^{-1}$ throughout all the calculations reported here (see below).

In order to illustrate multipolar absorption spectroscopy, we consider a graphene micro-ring with external radius b and an inner hole at the core with radius a (see Fig. 1a). Due to rotational invariance, radiation scattering by the micro-ring is accompanied by conservation of the component of angular momentum along the micro-ring axis, and hence it is convenient to consider an impinging field with a well-defined value of such component. Such an impinging field also allows to illustrate the detailed angular momentum exchanges between THz radiation and the molecule, and hence we assume that the graphene ring is illuminated by a left-handed circularly polarized monochromatic plane wave at normal incidence with electric field $\mathbf{E}_{\text{in}} = \text{Re}[E_0 e^{ik_0 z - i\omega t} \hat{\mathbf{e}}_{\text{L}}]$, where E_0 is the complex field amplitude, $k_0 = 2\pi/\lambda$, $\omega = k_0 c$, and $\hat{\mathbf{e}}_{\text{L}}$ is the complex unit vector of left circular polarization. We hereafter set $\lambda = 55.92 \mu\text{m}$ as the fixed vacuum wavelength, so that the photon energy $\hbar\omega$ is resonant with the $J = 0 \rightarrow J = 2$ rotational transition of H_2^+ (see below). Owing to the graphene discontinuity and the deep-subwavelength polarization⁴⁰, the spin–orbit interaction (SOI) of radiation provides a scattered field $\mathbf{E}_{\text{scat}}(\mathbf{r}, t) = \text{Re}[\mathbf{E}(\mathbf{r})e^{-i\omega t}]$ with amplitude

$$\begin{aligned} \mathbf{E}(\mathbf{r}) &= E_{\text{L}}(\mathbf{r})\hat{\mathbf{e}}_{\text{L}} + E_{\text{R}}(\mathbf{r})\hat{\mathbf{e}}_{\text{R}} + E_z(\mathbf{r})\hat{\mathbf{e}}_z \\ &= \tilde{E}_{\text{L}}(r_{\perp}, z)\hat{\mathbf{e}}_{\text{L}} + \tilde{E}_{\text{R}}(r_{\perp}, z)e^{2i\varphi}\hat{\mathbf{e}}_{\text{R}} + \tilde{E}_z(r_{\perp}, z)e^{i\varphi}\hat{\mathbf{e}}_z, \end{aligned} \quad (1)$$

where $\hat{\mathbf{e}}_{\text{R}}$ is the complex unit vector of right circular polarization, $\hat{\mathbf{e}}_z$ is the unit vector over the z direction, \mathbf{r}_{\perp} is the in-plane position vector with modulus r_{\perp} and azimuthal angle φ , and the components' amplitudes \tilde{E}_{L} , \tilde{E}_{R} , and \tilde{E}_z are functions only of r_{\perp} and z . We emphasize that the peculiar topological charges of the R and z components arise from radiation SOI under the conservation of the total angular momentum (graphene ring + radiation) along $\hat{\mathbf{e}}_z$ owing to cylindrical symmetry (see the Methods and Supplementary Note 1). Thus, the graphene ring acts as a nanogenerator of THz vortices in the different field components and, as we show below, such vortices play a crucial

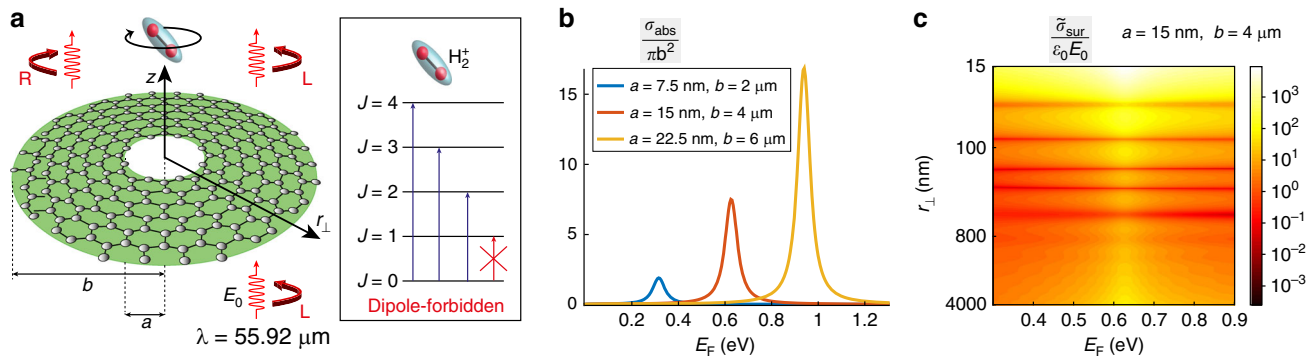


Fig. 1 Plasmon-enhanced multipolar absorption spectroscopy. **a** Schematic illustration of a graphene micro-ring of radius b with a nano-hole of radius a at the core surrounded by dipole-inactive molecules (in our calculations we considered H_2^+ for the sake of simplicity). The system is excited by an impinging THz wave of fixed vacuum wavelength $\lambda = 55.92 \mu\text{m}$, of amplitude E_0 and left circular polarization (L). The scattered radiation has both left and right (R) circularly polarized components. **b** Electrically tunable absorption cross-section σ_{abs} as a function of the Fermi energy (E_F) for several inner and outer radii and rescaled to the area of the outer circle πb^2 . **c** Dependence of the induced surface charge density $\tilde{\sigma}_{\text{sur}}$ rescaled to $\epsilon_0 E_0$ (where ϵ_0 is the vacuum dielectric permittivity) over the radius $a < r_{\perp} < b$ and E_F .

role in the enhancement of the molecule absorption cross-section over all orientations.

Depending on the inner and outer radii, the graphene ring sustains plasmon resonances at peculiar Fermi energies E_F where the absorption cross-section is maximum (see Fig. 1b). In order to achieve a strong plasmon resonance at an experimentally feasible Fermi energy, we hereafter set $a = 15 \text{ nm}$ and $b = 4 \mu\text{m}$ for which the resonance occurs at $E_F = 0.63 \text{ eV}$. Due to above discussed angular momentum conservation, the induced surface charge density over the graphene micro-ring has topological charge equal to the impinging angular momentum, i.e., $\sigma_{\text{sur}}(\mathbf{r}_{\perp}) = \tilde{\sigma}_{\text{sur}}(r_{\perp})e^{i\varphi}$. It is worth noting that, at the peculiar Fermi energy where electron oscillations are resonant, the radial part of the induced surface charge density $\tilde{\sigma}_{\text{sur}}$, as reported in Fig. 1c, is particularly large close to the inner ring edge (where $\tilde{\sigma}_{\text{sur}} \simeq 9000 \epsilon_0 E_0$) entailing a very strong and rapidly varying scattered field inside the ring nano-hole (see Supplementary Note 2 and Supplementary Fig. 1).

Owing to the resonant excitation, the scattered field is much larger than the impinging field $|\mathbf{E}| \gg E_0$, see Fig. 2a–c, where we plot the field profile of every component at resonance, at different distances from the micro-ring. Note that, thanks to the excitation of graphene plasmons in the ring, the THz wave gets squeezed at the nanoscale and it also displays spatial features whose scale is comparable with the molecular scale, as shown in the three insets. The peculiar topological charges of the field components R and z are responsible for their vortex-like structures, which are observed as an azimuthal angle periodicity of imaginary (or real) part of their field amplitudes (see Figs. 2d–f). Note that the inner edge of the graphene ring produces a local field intensity enhancement of the order $|\mathbf{E}/E_0| \simeq 10^6$, while at the outer edge $|\mathbf{E}/E_0| \simeq 10^3$, which is consistent with previously reported results⁴⁷.

Plasmon-assisted multipolar absorption spectroscopy. In general, multipolar absorption is inherently small because it ensues from the electromagnetic field spatial variation within the molecule¹⁹. However, over recent years it has been shown that such “forbidden” transitions can be accessed by the deep-subwavelength scattered field produced by graphene nanostructures^{47–55}. Note in Figs. 2a–c that the sharp peak at the inner ring radius produces spatial features of the THz scattered wave that are of the order of $\simeq 1 \text{ \AA}$ (see Supplementary Note 2, where we report analytical approximations of the sharp peak in terms of elliptic integrals). Thus, multipolar absorption is expected to be

particularly efficient for molecules nearby the inner ring radius. Such a peculiar feature of graphene thus opens otherwise precluded possibilities for multipolar terahertz absorption sensing. Indeed, in the far-infrared and terahertz regions of the electromagnetic spectrum molecules typically possess purely-rotational transitions, while purely vibrational or mixed roto-vibrational transitions typically happen in the mid-infrared¹⁹. In order to illustrate plasmon-assisted multipolar absorption spectroscopy, we consider the simplest homonuclear diatomic molecule (dipole inactive), i.e., ionized molecular hydrogen H_2^+ , which possesses rotational energy levels $E_J = BJ(J+1)$, where $B = 29.8 \text{ cm}^{-1}$ (see the Methods and Supplementary Note 2). We investigate the molecule–radiation interaction by resorting to the Power–Zienau–Woolley scheme⁵⁶, whose interaction Hamiltonian is $H_I = -\int d^3\mathbf{r} \mathbf{P}(\mathbf{r}) \cdot \mathbf{E}(\mathbf{r}, t)$ where $\mathbf{E}(\mathbf{r}, t)$ is the total electric field around the graphene disk and $\mathbf{P}(\mathbf{r})$ is the molecule polarization density. By solving perturbatively the density matrix equations of the molecule with such an interaction Hamiltonian in principle enables the calculation the molecular absorption cross-section σ_{mol} accounting for all multipolar transitions (see the Methods section and Supplementary Note 2).

Discussion

For quadrupole transitions, averaging over all possible molecular orientations accounted by the azimuthal quantum number M , we obtain the results in Fig. 3, where in (a) we depict the dependence of the plasmon-enhanced molecule absorption cross-section σ_{mol} over the in-plane radius r_{\perp} and altitude z , while in (b) we illustrate the altitude dependence of $\langle \sigma_{\text{mol}} \rangle$ averaged over the disk $z = z_0$, $0 \leq r_{\perp} \leq b$. Both the absorption cross-section and its average on the disk are rescaled to the absorption cross-section of molecules in vacuum σ_{vac} . Note in Fig. 3a that graphene enhances the quadrupolar transition cross-section by 16 orders of magnitude locally for molecules nearby the inner graphene edge. The enhancement factor reduces for radii $a < r_{\perp} < b$, but the minimum is 10^4 . At the outer radius $r_{\perp} = b$, the enhancement factor rises again sharply owing to the high field gradient provided by the graphene edge discontinuity and reaches 10^9 . The overall performance of the plasmon-enhanced spectroscopic technique is evaluated through the averaged enhancement factor $\langle \sigma_{\text{mol}} \rangle / \sigma_{\text{vac}}$, which ranges from 10^6 to 10^9 for molecules at altitudes between 1 nm and 50 nm (see Fig. 3b). We emphasize that such an enhancement factor is averaged over all molecular orientations and nevertheless it remains large due to the electromagnetic SOI enabling an efficient vortex generation over the right circular

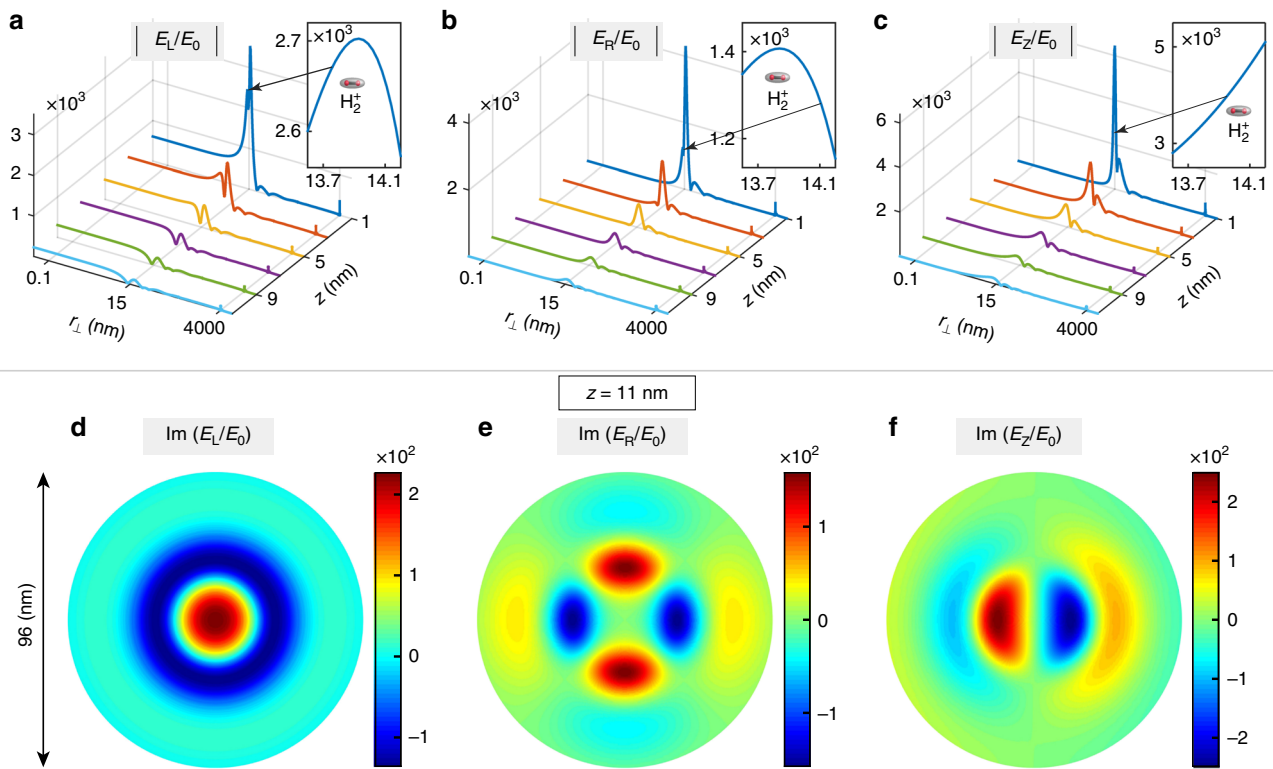


Fig. 2 Near-field features of the scattered field by the graphene micro-ring. The scatterer micro-ring has inner and outer radii $a = 15 \text{ nm}$ and $b = 4 \mu\text{m}$, respectively, its Fermi energy is $E_F = 0.63 \text{ eV}$ and the radiation wavelength is $\lambda = 55.92 \mu\text{m}$. **a-c** Dependence of the scattered field amplitudes E_L , E_R , and E_z over the in-plane radius r_{\perp} and the altitude z . Note the large field enhancement $|\mathbf{E}| \gg E_0$ accompanying resonant scattering, enhancement which is particularly marked close to the inner edge $r_{\perp} = 15 \text{ nm}$ of the micro-ring where the scattered field components are three order of magnitude greater than impinging field amplitude. Note also that the scattered field has deep-subwavelength features whose spatial scale is comparable with the H_2^+ spatial extension, as shown in the three insets where the molecules are drawn with their actual size (with respect to the r_{\perp} axis). **d-f** Contour plots of the imaginary parts of the scattered field amplitudes E_L , E_R , and E_z rescaled to the impinging amplitude, at the plane $z = 11 \text{ nm}$ out of micro-ring. Note that the azimuthal angle periodicity of such plots is due to the topological charges 0, 2, and 1 of the three field components, respectively

polarization and longitudinal components (see Fig. 2; Supplementary Note 2).

We note that the only component of the angular momentum conserved is the projection over the z -axis J_z . The system radiation+molecule is invariant under rotations around the z -axis only for molecules positioned over the z -axis. Thus, angular momentum conservation implies that for $r_{\perp} = 0$ the only transitions $J \rightarrow J + 2, M \rightarrow M + 1$ are allowed, which we obtain analytically (see Supplementary Note 2). Conversely, off-axis molecules are driven by a THz field that is not rotationally invariant over their axis, and thus all transitions $J \rightarrow J + 2, M \rightarrow 0, M \pm 1, M \pm 2$ are ignited.

A relevant practical aspect of the proposed sensing technique lies in the electrical control of the graphene Fermi energy, which allows the fine tuning of the desired plasmon resonance to match the molecule rotational transition. This requires a gating device such that a gate at the bottom is combined with a contact for the graphene ring. For instance, electrical connection may be attained by a thin transparent insulating layer, an approach that has already been exploited for the active control of graphene disk plasmons⁵⁷.

Our calculations demonstrate that enhanced multipolar THz absorption spectroscopy can be attained through graphene plasmons, which enable to identify the chemical species of dipole-inactive adsorbed molecules. The enhancement factor of the molecular absorption cross-section locally reaches values as high as 10^{16} , while in average lies between 10^7 and 10^9 , depending on the altitude of the molecule with respect to the graphene area. We

envisage that our findings are relevant in a number of other sensing applications in the THz and far-infrared, as in particular Raman spectroscopy. Furthermore, the strong SOI of radiation mediated by graphene acts as a nanogenerator of electromagnetic vortices that plays a key role for chiral sensing of molecule enantiomers. Graphene enhanced multipolar terahertz absorption spectroscopy can potentially open disruptive applications in pharmaceutical sciences.

Methods

Scattering of radiation with well-defined angular momentum by a graphene micro-ring. In the presence of the impinging plane wave $\mathbf{E}^{(i)}(\mathbf{r}) = \mathbf{E}_0 e^{ik_0 z}$ ($k_0 = \omega/c$), the graphene micro-ring at the plane $z = 0$ scatters the field $\mathbf{E}(\mathbf{r})$ satisfying, in the long-wavelength limit, the equation

$$\mathbf{E}(\mathbf{r}) = \mathbf{E}_0 e^{ik_0 z} + \frac{i\sigma}{4\pi\epsilon_0\omega} \nabla \int d^2\mathbf{r}'_{\perp} \frac{\nabla'_{\perp} \cdot [f(r'_{\perp})\mathbf{E}_{\perp}(r'_{\perp})]}{\sqrt{|\mathbf{r}_{\perp} - \mathbf{r}'_{\perp}|^2 + z^2}} \quad (2)$$

where σ is the graphene surface conductivity at frequency ω , $\mathbf{r}_{\perp} = x\hat{\mathbf{e}}_x + y\hat{\mathbf{e}}_y$, $\mathbf{E}_{\perp}(\mathbf{r}_{\perp}) = E_x(\mathbf{r}_{\perp})\hat{\mathbf{e}}_x + E_y(\mathbf{r}_{\perp})\hat{\mathbf{e}}_y$ is the transverse component of the electric field on the ring, $\nabla_{\perp} = \frac{\partial}{\partial x}\hat{\mathbf{e}}_x + \frac{\partial}{\partial y}\hat{\mathbf{e}}_y$, and $f(r_{\perp})$ is the ring geometrical filling factor which is equal to zero if $r_{\perp} < a$ or $r_{\perp} > b$ and it is equal to one if $a + \delta < r_{\perp} < b - \delta$, where δ is a suitable edge layer thickness⁵⁸. The electrostatic approximation allows one to introduce the potential $V(\mathbf{r}_{\perp})$ for the electric field produced by the ring on itself according to $\mathbf{E}_{\perp}(\mathbf{r}_{\perp}) = \mathbf{E}_0 - \nabla_{\perp} V(\mathbf{r}_{\perp})$ and Eq. (2) turns into a scalar integral equation for $V(\mathbf{r}_{\perp})$ (see Supplementary Note 2). Due to the ring rotational invariance, the z - component of the radiation angular momentum is conserved upon scattering, so that the choice of an impinging plane wave with well-defined angular momentum entails a dimensionality reduction of the scattering problem. Specifically, we have chosen a left hand circularly polarized impinging plane wave with $\mathbf{E}_0 = E_0\hat{\mathbf{e}}_L$, which has angular momentum equal to one and, as shown in the

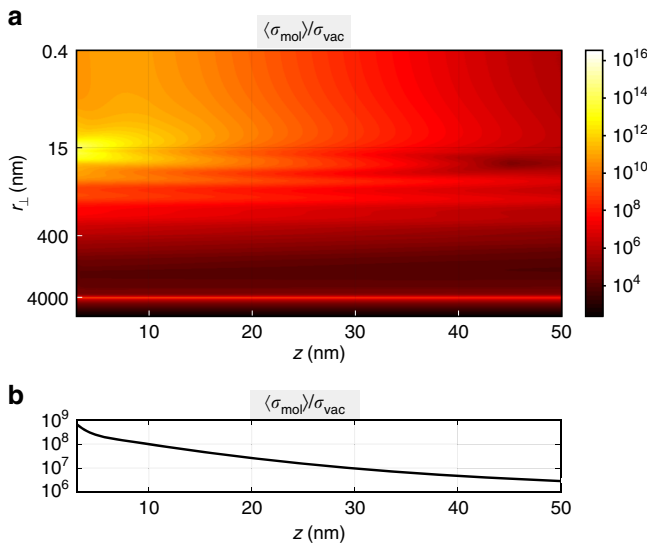


Fig. 3 Molecular absorption cross-section enhancement. The considered absorption rotational transition of H_2^+ is $J_i = 0 \rightarrow J_f = 2$ and the absorbed photon energy is $\hbar\omega = E_f - E_i = 6B \simeq 178.8 \text{ cm}^{-1}$ in turn corresponding to the wavelength $\lambda = 55.92 \text{ }\mu\text{m}$, which we have consistently used in the electromagnetic scattering design. **a** Contour plot of the plasmon-enhanced molecule absorption cross-section σ_{mol} rescaled to the cross-section of molecules in vacuum σ_{vac} averaged over all molecular orientations as a function of the in-plane radius r_{\perp} and altitude z . **b** Plasmon-enhanced molecule absorption cross-section averaged over the disk $z = z_0$, $0 \leq r_{\perp} \leq b$, $\langle \sigma_{\text{mol}} \rangle$, rescaled to σ_{vac} as a function of the altitude z_0

Supplementary Note 1, this implies that the electrostatic potential has a definite topological charge equal to the radiation angular momentum, i.e.,

$$V(\mathbf{r}_{\perp}) = \tilde{V}(r_{\perp})e^{i\varphi}. \quad (3)$$

Accordingly, the electric field generated by such potential has the general form as in Eq. (1) and the radial part $\tilde{V}(r_{\perp})$ satisfies a one-dimensional integral equation on the interval $a < r_{\perp} < b$, which we have numerically solved resorting to representation theory (see Supplementary Note 1). Once the potential is evaluated on the ring, Eq. (2) yields the scattered electric field (in the near-field) which formally coincides with the field produced by the surface charge density $\sigma_{\text{sur}}(\mathbf{r}_{\perp}) = -\frac{\hbar\omega}{\omega} \nabla_{\perp} \cdot [f(r_{\perp})\mathbf{E}_{\perp}(\mathbf{r}_{\perp}, 0)]$ which, due to conservation of angular momentum, has a well-defined topological charge in turn equal to the radiation angular momentum, i.e.,

$$\sigma_{\text{sur}}(\mathbf{r}_{\perp}) = \tilde{\sigma}_{\text{sur}}(r_{\perp})e^{i\varphi}. \quad (4)$$

Interaction of the scattered field with hydrogen molecular ions. We have investigated the molecule–radiation interaction by means of the Power–Zienau–Woolley⁵⁶ scheme according to which the interaction hamiltonian is

$$H_I = - \int d^3\mathbf{r} \mathbf{P}(\mathbf{r}) \cdot \mathbf{E}(\mathbf{r}, t), \quad (5)$$

where $\mathbf{E}(\mathbf{r}, t) = \text{Re}[\mathbf{E}(\mathbf{r})e^{-i\omega t}]$ is the real electric field and $\mathbf{P}(\mathbf{r})$ is the polarization density which, for a system of point charges (of charge q_{α} and located at \mathbf{r}_{α}) localized around the point $\bar{\mathbf{R}}$, is

$$\mathbf{P}(\mathbf{r}) = \sum_{\alpha} q_{\alpha}(\mathbf{r}_{\alpha} - \bar{\mathbf{R}}) \int_0^1 du \delta[\mathbf{r} - \bar{\mathbf{R}} - u(\mathbf{r}_{\alpha} - \bar{\mathbf{R}})]. \quad (6)$$

The analysis of the quadrupolar absorption spectroscopy is based on the Taylor expansion of the electric field up to the first-order around the molecule center of the mass. As shown in the Supplementary Note 2, the probability amplitude $M_{\bar{n}}$ of the transition $(n, J_i, M_i) \rightarrow (n, J_f, M_f)$, where (n, J, M) are the molecule vibrational, rotational, and magnetic quantum numbers, respectively, is

$$M_{\bar{n}} = I_{J_i J_f; n} \sum_{q=-2}^2 \langle 2, J_i; q, M_i | J_f, M_f \rangle V^q \quad (7)$$

where $I_{J_i J_f; n}$ is independent on the field, $\langle j_1, j_2; m_1, m_2 | j_3, m_3 \rangle$ are the Clebsch–Gordan coefficients and V^q are the five spherical components of the

field gradient tensor $\partial_i E_j$ evaluated at the molecule center of the mass. Conservation of angular momentum upon scattering from the ring implies that they have defined topological charge

$$V^q(r_{\perp}, \varphi, z) = \tilde{V}^q(r_{\perp}, z)e^{i(1-q)\varphi}. \quad (8)$$

The absorption cross-section of the transition $J_i \rightarrow J_f = J_i + 2$ is (see Supplementary Note 2)

$$\sigma_{\text{mol}}(r_{\perp}, z) = g |I_{J_i J_f; n}|^2 \sum_{q=-2}^2 w_q^{(J_i)} |\tilde{V}^q(r_{\perp}, z)|^2 \quad (9)$$

where g is a constant and $w_q^{(J_i)} = \sum_{M_i=-J_i}^{J_i} \langle 2, J_i; q, M_i | J_i + 2, M_i + q \rangle^2$. The absorption cross-section in the absence of the graphene ring, is

$$\sigma_{\text{vac}} = g |I_{J_i J_f; n}|^2 w_1^{(J_i)} |k_0 E_0|^2. \quad (10)$$

so that the efficiency of the graphene ring of enhancing the rotational absorption cross-section of a molecule quantified by the ratio

$$\frac{\sigma_{\text{mol}}(r_{\perp}, z)}{\sigma_{\text{vac}}} = \sum_{q=-2}^2 \frac{w_q^{(J_i)} |\tilde{V}^q(r_{\perp}, z)|^2}{w_1^{(J_i)} |k_0 E_0|^2}. \quad (11)$$

Data availability

The data and codes that support the findings of this study are available from the corresponding authors on request.

Received: 9 May 2019 Accepted: 22 August 2019

Published online: 16 September 2019

References

- Huber, R. et al. How many-particle interactions develop after ultrafast excitation of an electron-hole plasma. *Nature* **414**, 286–289 (2001).
- Kaindl, R. A., Carnahan, M. A., Hagele, D., Lovenich, R. & Chemla, D. S. Ultrafast terahertz probes of transient conducting and insulating phases in an electron-hole gas. *Nature* **423**, 734–738 (2003).
- Cooke, D. G. et al. Transient terahertz conductivity in photoexcited silicon nanocrystalline films. *Phys. Rev. B* **73**, 193311 (2006).
- Leinß, S. et al. Terahertz coherent control of optically dark paraexcitons in Cu_2O . *Phys. Rev. Lett.* **101**, 246401 (2008).
- Walther, M., Fischer, B. M. & Jepsen, P. U. Noncovalent intermolecular forces in polycrystalline and amorphous saccharides in the far infrared. *Chem. Phys.* **288**, 261–268 (2003).
- Beard, M. C., Turner, G. M. & Schmuttenmaer, C. A. Measuring intramolecular charge transfer via coherent generation of THz radiation. *J. Phys. Chem. A* **106**, 878–883 (2002).
- Korter, T. M. & Plusquellic, D. F. Continuous-wave terahertz spectroscopy of biotin: vibrational anharmonicity in the far-infrared. *Chem. Phys. Lett.* **385**, 45–51 (2004).
- Allis, D. G., Fedor, A. M., Korter, T. M., Bjarnason, J. E. & Brown, E. R. Assignment of the lowest-lying THz absorption signatures in biotin and lactose monohydrate by solid-state density functional theory. *Chem. Phys. Lett.* **440**, 203–209 (2007).
- Zhang, H., Siegrist, K., Plusquellic, D. F. & Gregurick, S. K. Terahertz spectra and normal mode analysis of the crystalline VA class dipeptide nanotubes. *J. Am. Chem. Soc.* **130**, 17846–17857 (2008).
- Whitmire, S. E. et al. Protein flexibility and conformational state: a comparison of collective vibrational modes of wild-type and D96N bacteriorhodopsin. *Biophys. J.* **85**, 1269–1277 (2003).
- Markelz, A. G., Knab, J. R., Chen, J. Y. & He, Y. F. Protein dynamical transition in terahertz dielectric response. *Chem. Phys. Lett.* **442**, 413–417 (2007).
- He, Y. F., Ku, P. I., Knab, J. R., Chen, J. Y. & Markelz, A. G. Protein dynamical transition does not require protein structure. *Phys. Rev. Lett.* **101**, 178103 (2008).
- Sim, Y. C., Maeng, I. & Son, J.-H. Frequency-dependent characteristics of terahertz radiation on the enamel and dentin of human tooth. *Curr. Appl. Phys.* **9**, 946–949 (2009).
- Lancaster, P. et al. Surfing the spectrum—what is on the horizon? *Br. Dent. J.* **215**, 401–409 (2013).
- Davies, A. G., Burnett, A. D., Fan, W., Linfield, E. H. & Cunningham, J. E. Terahertz spectroscopy of explosives and drugs. *Mater. Today* **11**, 18–26 (2008).
- Allis, D. G., Hakey, P. M. & Korter, T. M. The solid-state terahertz spectrum of MDMA (Ecstasy)—a unique test for molecular modeling assignments. *Chem. Phys. Lett.* **463**, 353 (2008).

17. Hakey, P. M., Allis, D. G., Ouellette, W. & Korter, T. M. Cryogenic terahertz spectrum of (-)-methamphetamine hydrochloride and assignment using solid-state density functional theory. *J. Phys. Chem. A* **113**, 5119–5127 (2009).
18. Hakey, P. M., Allis, D. G., Hudson, M. R., Ouellette, W. & Korter, T. M. Investigation of (1R,2S)-(-)-ephedrine by cryogenic terahertz spectroscopy and solid-state density functional theory. *Chem. Phys. Chem.* **10**, 2434–2444 (2009).
19. Wollrab, J. E. & Loebl, E. M. *Rotational Spectra and Molecular Structure: Physical Chemistry: A Series of Monographs* (Academic Press, New York, 2016).
20. Moskovits, M. Surface-enhanced spectroscopy. *Rev. Mod. Phys.* **57**, 783–826 (1985).
21. Moskovits, M. Surface-enhanced Raman spectroscopy: a brief retrospective. *J. Raman Spectrosc.* **36**, 485–496 (2005).
22. Kneipp, K. et al. Single molecule detection using surface-enhanced Raman scattering (SERS). *Phys. Rev. Lett.* **78**, 1667–1670 (1997).
23. Nie, S. & Emory, S. R. Probing single molecules and single nanoparticles by surface-enhanced Raman scattering. *Science* **275**, 1102–1106 (1997).
24. Rodríguez-Lorenzo, L. et al. Zeptomol detection through controlled ultrasensitive surface-enhanced Raman scattering. *J. Am. Chem. Soc.* **131**, 4616–4618 (2009).
25. Leuversing, J. H. W. U.S. Patent US4. 313–734 (1982).
26. Lin, D. et al. Label-free detection of blood plasma using silver nanoparticle based surface-enhanced Raman spectroscopy for esophageal cancer screening. *J. Biomed. Nanotechnol.* **10**, 478–484 (2014).
27. Ueno, K., Nozawa, S. & Misawa, H. Surface-enhanced terahertz spectroscopy using gold rod structures resonant with terahertz waves. *Opt. Express* **23**, 28584–28592 (2015).
28. Hwang, E. H. & Das Sarma, S. Dielectric function, screening, and plasmons in two-dimensional graphene. *Phys. Rev. B* **75**, 205418 (2007).
29. Ju, L. et al. Graphene plasmonics for tunable terahertz metamaterials. *Nat. Nanotechnol.* **6**, 630–634 (2011).
30. Chen, J. et al. Optical nano-imaging of gate-tunable graphene plasmons. *Nature* **487**, 77–81 (2012).
31. Fei, Z. et al. Gate-tuning of graphene plasmons revealed by infrared nano-imaging. *Nature* **487**, 82–85 (2012).
32. Yan, H. et al. Tunable infrared plasmonic devices using graphene/insulator stacks. *Nat. Nanotechnol.* **7**, 330–334 (2012).
33. Low, T. & Avouris, P. Graphene plasmonics for terahertz to mid-infrared applications. *ACS Nano* **8**, 1086–1101 (2014).
34. Wu, L., Chu, H. S., Koh, W. S. & Li, E. P. Highly sensitive graphene biosensors based on surface plasmon resonance. *Opt. Express* **18**, 14395–14400 (2010).
35. Xu, W. et al. Surface enhanced Raman spectroscopy on a flat graphene surface. *Proc. Natl Acad. Sci. USA* **109**, 9281–9286 (2012).
36. Li, Y. et al. Graphene plasmon enhanced vibrational sensing of surface-adsorbed layers. *Nano Lett.* **14**, 1573–1577 (2014).
37. Francescato, Y., Giannini, V., Yang, J., Huang, M. & Maier, S. A. Graphene sandwiches as a platform for broadband molecular spectroscopy. *ACS Photonics* **1**, 437–443 (2014).
38. Marini, A., Silveiro, I. & García de Abajo, F. J. Molecular sensing with tunable graphene plasmons. *ACS Photonics* **2**, 876–882 (2015).
39. Rodrigo, D. et al. Mid-infrared plasmonic biosensing with graphene. *Science* **349**, 165–168 (2015).
40. Ciattoni, A., Rizza, C., Lee, H. W. H., Conti, C. & Marini, A. Plasmon-enhanced spin-orbit interaction of light in graphene. *Laser & Photon. Rev.* **12**, 1800140 (2018).
41. Williams, C. R. et al. Highly confined guiding of terahertz surface plasmon polaritons on structured metal surfaces. *Nat. Photon.* **2**, 175–179 (2008).
42. Nikitin, A. Y., Guinea, F., García-Vidal, F. J. & Martín-Moreno, L. Edge and waveguide terahertz surface plasmon modes in graphene microribbons. *Phys. Rev. B* **84**, 161407 (R) (2011).
43. Giovannetti, G. et al. Doping graphene with metal contacts. *Phys. Rev. Lett.* **101**, 026803 (2008).
44. Grigorenko, A. N., Polini, M. & Novoselov, K. S. Graphene plasmonics. *Nat. Photon.* **6**, 749–758 (2012).
45. García de Abajo, F. J. Graphene plasmonics: challenges and opportunities. *ACS Photon.* **1**, 135–152 (2014).
46. Ni, G. X. et al. Fundamental limits to graphene plasmonics. *Nature* **557**, 530–533 (2018).
47. Sanders, S., May, A., Alabastri, A. & Manjavacas, A. Extraordinary enhancement of quadrupolar transitions using nanostructured graphene. *ACS Photon.* **5**, 3282–3290 (2018).
48. Rivera, N., Kammer, I., Zhen, B., Joannopoulos, J. D. & Soljacic, M. Shrinking light to allow forbidden transitions on the atomic scale. *Science* **353**, 263–269 (2016).
49. Manjavacas, A. et al. Magnetic light and forbidden photochemistry: the case of singlet oxygen. *J. Mater. Chem. C* **5**, 11824–11831 (2017).
50. Minamimoto, H., Oikawa, S., Li, X. & Murakoshi, K. Plasmonic fields focused to molecular size. *ChemNanoMat* **3**, 843–856 (2017).
51. Sloan, J., Rivera, N., Soljacic, M. & Kammer, I. Tunable UV-emitters through graphene plasmonics. *Nano Lett.* **18**, 308–313 (2018).
52. Cuartero-Gonzalez, A. & Fernandez-Dominguez, A. I. Light-forbidden transitions in plasmon-emitter interactions beyond the weak coupling regime. *ACS Photon.* **5**, 3415–3420 (2018).
53. Machado, F., Rivera, N., Buljan, H., Soljacic, M. & Kammer, I. Shaping polaritons to reshape selection rules. *ACS Photon.* **5**, 3064–3072 (2018).
54. Fan, Y. et al. Photoexcited graphene metasurfaces: significantly enhanced and tunable magnetic resonances. *ACS Photon.* **5**, 1612–1618 (2018).
55. Fan, Y. et al. Graphene plasmonics: a platform for 2D optics. *Adv. Opt. Mater.* **7**, 1800537 (2019).
56. Cohen-Tannoudji, C., Dupont-Roc, J. & Grynberg, G. *Photons and Atoms: Introduction to Quantum Electrodynamics* (Wiley-VCH, 1997).
57. Fang, Z. et al. Gated tunability and hybridization of localized plasmons in nanostructured graphene. *ACS Nano* **7**, 2388–2395 (2013).
58. Wang, W., Apell, P. & Kinaret, J. Edge plasmons in graphene nanostructures. *Phys. Rev. B* **84**, 085423 (2011).

Acknowledgements

A.C. acknowledges the U.S. Army International Technology Center Atlantic for financial support (grant number W911NF-14-1-0315). C.C. acknowledges the H2020 QuantERA Quomplex project (grant number 731743). A.M. acknowledges support from the Rita Levi Montalcini Fellowship (grant number PGR15PCCQ5) funded by the Italian Ministry of Education, Universities and Research (MIUR). We acknowledge the PRIN 2017 Project no. 20177PCKT.

Author contributions

A.M. and A.C. conceived the idea and developed the approach. A.C. carried out the analytical analysis and performed the numerical simulations. A.M., A.C. and C.C. discussed the results and wrote the paper.

Additional information

Supplementary information accompanies this paper at <https://doi.org/10.1038/s42005-019-0213-x>.

Competing interests: The authors declare no competing interests.

Reprints and permission information is available online at <http://npg.nature.com/reprintsandpermissions/>

Publisher's note Springer Nature remains neutral with regard to jurisdictional claims in published maps and institutional affiliations.



Open Access This article is licensed under a Creative Commons Attribution 4.0 International License, which permits use, sharing, adaptation, distribution and reproduction in any medium or format, as long as you give appropriate credit to the original author(s) and the source, provide a link to the Creative Commons license, and indicate if changes were made. The images or other third party material in this article are included in the article's Creative Commons license, unless indicated otherwise in a credit line to the material. If material is not included in the article's Creative Commons license and your intended use is not permitted by statutory regulation or exceeds the permitted use, you will need to obtain permission directly from the copyright holder. To view a copy of this license, visit <http://creativecommons.org/licenses/by/4.0/>.

© The Author(s) 2019